UNIVERSITY OF CALGARY

Towards non-destructive detection of photonic qubits

using a rare-earth-ion doped crystal

by

Chetan Deshmukh

A THESIS

SUBMITTED TO THE FACULTY OF GRADUATE STUDIES

IN PARTIAL FULFILLMENT OF THE REQUIREMENTS FOR THE

DEGREE OF MASTER OF SCIENCE

GRADUATE PROGRAM IN PHYSICS AND ASTRONOMY

CALGARY, ALBERTA

February, 2017

Abstract

Non-destructive detection of photonic qubits is an enabling technology for quantum information processing and quantum communication. For practical applications such as quantum repeaters and networks, it is desirable to implement such detection in a way that allows some form of multiplexing as well as easy integration with other components such as solid-state quantum memories. Here we propose an approach to non-destructive photonic qubit detection that promises to have all the mentioned features. Mediated by an impurity-doped crystal, a signal photon in an arbitrary time-bin qubit state modulates the phase of an intense probe pulse that is stored during the interaction. Using a thulium-doped waveguide in $LiNbO_3$, we perform a proof-of-principle experiment with macroscopic signal pulses, demonstrating the expected cross-phase modulation as well as the ability to preserve the coherence between temporal modes. Our findings open the path to a new key component of quantum photonics based on rare-earth-ion doped crystals.

Acknowledgements

First of all, I would like to thank my supervisor Dr. Wolfgang Tittel for giving me the opportunity to join his group and to work in his laboratory. I learnt a lot about experimental physics from our numerous discussions and I hope I have absorbed a little of his immense knowledge and wisdom. He has been a great mentor - pushing us to do challenging work when needed, while being very supportive when things weren't going great.

I am also deeply indebted to Neil and Daniel, my two lab-mates-cum-mentors, for making me feel very welcome in the lab. They showed me how first-rate experimental physics is done on the ground, and a lot of what I know today about experimental techniques is due to them. Also, thank you Neil for all the brainstorming sessions and for helping me write this thesis. I would also like to thank Marcel-li and Gabriel for teaching me a little bit about single-photon sources. I don't think I will ever forget Marcel-li's trademark pump-signal-idler bandwidth diagram. I am also thankful to Raju, Mohsen, Qiang, Thomas, Lucile, Pascal and Erhan for being great co-workers and also for their friendship.

Many thanks also to Dr. Christoph Simon, with whom I had the privilege to collaborate on several projects. The theoretical insight that I got from discussions with him, Khabat, Parisa, Sandeep and Sumit have helped improve my understanding about a lot of things.

Finally, I would like to thank my family for giving me the freedom to pursue my dreams. I know it hasn't been easy for them, sometimes not speaking with me for weeks, and I will always be indebted for all the sacrifices they have done for me.

Table of Contents

List of Figures and Illustrations

List of Symbols, Abbreviations and Nomenclature

Symbol	Definition
QIS	Quantum Information Science
QIP	Quantum Information Processing
AFC	Atomic Frequency Comb
CQED	Cavity Quantum Electrodynamics
EIT	Electromagnetically Induced Transparency
RWA	Rotating Wave Approximation
REI	Rare-Earth-Ion
MEMS	Micro Electro-Mechanical Switches
RF	Radio Frequency
PM	Phase Modulator
AOM	Acousto Optic Modulator
LO	Local Oscillator

Chapter 1

Introduction

Systems at sub-microscopic scales are governed by the laws of quantum mechanics and exhibit many interesting, and sometimes non-intuitive, properties that are very different from those of macroscopic 'classical' systems. For example, the measurement outcome of a physical property of a system that obeys quantum mechanics can be probabilistic. These systems can simultaneously be in several states, each of which is probable depending on the type of measurement. This is unlike classical systems, which are always in well-defined states. This property of a quantum system is called 'superposition' and it has been at the foundation of quantum mechanics ever since its development. Quantum systems are hence described using a wavefunction, which is a mathematical function that provides the probability amplitudes for the various outcomes of a measurement of a physical property of the system. Quantum entanglement is another such property that manifests when the physical properties of two or more systems depend on each other and the joint state cannot be described by attributing independent states to each system.

Quantum information science (QIS) involves the study of these properties for developing potential novel applications. The basic unit of information in the classical domain is called a bit, which can either be 0 or 1. The analogue of a bit in QIS is called a qubit and it can simultaneously be in state $|0\rangle$ and state $|1\rangle$ with, say, complex probability amplitudes α and β respectively, where $|\alpha|^2 + |\beta|^2 = 1$. The wavefunction can be described as $\alpha|0\rangle + \beta|1\rangle$. Encoding information in qubits has led to many unique applications including quantum computing [2], which promises to solve certain computational problems that are beyond the reach of classical computers, quantum communication [3, 4], which guarantees unconditionally secure transmission of information, and quantum metrology [5, 6], which allows the development of high-precision measurement devices. All of these applications can be envisaged to form operational nodes linked to each other in a future

quantum internet [7], which can accomplish tasks that are impossible with classical architectures.

An experimental implementation of these proposed applications places three main demands on the physical realization. Firstly, it should provide qubits that are easy to manipulate so that the required quantum information can be mapped and operated upon easily. Secondly, the qubit should preserve the encoded quantum information for as long as needed. In other words, the qubit should be free of 'decoherence'. Thirdly, there should be a way for connecting two qubits so that conditional two-qubit operations can be performed. Many physical realizations have been proposed that satisfy the above three conditions to various degrees. Photons, which are elementary particles of light, have been an integral part of many of the proposed physical architectures. This is mainly because they simultaneously allow encoding of quantum information and are free of decoherence. This has led to proposals that use photons as qubits by encoding quantum information in various degrees of freedom, hence forming the building-blocks of photon-based quantum computing architectures [8], as well as ones that use photons for carrying quantum information for the purpose of quantum communication [9].

Many of these quantum photonic applications require the presence of a precise number of photons to operate successfully [10]. It would hence be very desirable to have a detection mechanism that heralds the presence of a photonic qubit so that precious quantum resources (say entangled photon pairs for quantum teleportation [11]), are used only when required (e.g. if the signal photons whose state is to be teleported are actually there). This is all the more essential in situations of significant loss, such as for quantum repeaters [12]. Standard absorbing detectors can't be used for this purpose as they end up destroying the photon along with the encoded information. We would hence need a detector that not only preserves the photon (by not absorbing it) but also does the projection measurement without affecting the encoded information. Such a measurement, which is referred to as a 'non-destructive' measurement [13], could then be used to detect photonic qubits, where the quantum information can be encoded in the degrees of freedom that are not affected by the projection measurement (e.g. in time-bin states or polarization states for the above case).

1.1 Some promising approaches to non-destructive photon detection

Several approaches to non-destructive measurement of a photon are currently being pursued. Using single laser-trapped atoms in high-finesse cavities, where the strong coupling between the atom and the cavity field gives rise to cavity quantum electrodynamics (CQED) phenomena, non-destructive detection of photons has recently been achieved [14]. The atom is initially prepared in a superposition of two states, whose phase is toggled if a photon impinges and then reflects off the atom-cavity system. By detecting the final phase of the atom, the presence (impinging) of a photon can be assessed. Using a similar setup, heralded storage of photonic qubits was also recently demonstrated [15]. When combined with readout, this is equivalent to non-destructive qubit detection.

Another approach involves using the interaction of the photon that is to be non-destructively measured (called the 'signal') with another photon (called the 'probe'), which is mediated by a non-linear medium. In a pioneering CQED experiment, again with single atoms in cavities, Kimble et al. demonstrated a large cross-phase modulation between the signal and probe photons with slightly different frequencies that were co-propagating in the atom-cavity system. This approach is also being pursued with atomic ensembles by 'slowing light' (and eventually storing it) using electromagnetically induced transparency (EIT) [16]. Large single-photon phase shifts mediated by laser-cooled atomic vapour have recently been reported using Rydberg blockade [17]. This experiment relies on the fact that when a single excitation is stored in one of the Rydberg states using EIT, the strong long-range dipole-dipole interaction between Rydberg atoms [18] results in the probe photon that traverses the medium afterwards to experience a different refractive index than if the signal photon was not stored. Using laser-cooled atoms coupled to a high-finesse cavity, large cross-phase modulations have also been reported using the AC Stark shift [19]. In this experiment, the probe is stored as an atomic coherence between the ground state and one of the hyperfine levels following which the signal, which is resonant with the cavity but slightly off-resonant with the transition between the hyperfine level and an additional excited state, induces an AC stark shift [20, 21]. This results in the probe acquiring a phase shift. This system has furthermore enabled

partial non-destructive detection of travelling photons [22]. These investigations are part of the general drive of using atomic ensembles to mediate strong photon-photon interactions [23]. Experimental realizations of photon-photon interaction using Rydberg states [24, 25, 26], and the AC Stark shift [27, 28] have furthermore enabled applications such as all-optical switching [29, 30].

As is evident from all the above work, single atoms and cold atomic gases constitute the most advanced experimental platforms targeting the detection of optical photons. However, from the point of view of practical applications, it is of interest to investigate implementations in the solid state as well. Ideally, such approaches should preserve the qubit state encoded into the photon, allow for multiplexing, and be compatible with existing solid-state quantum information processing and communication components. Here we propose a scheme for non-destructive detection of photonic time-bin qubits that has all of these characteristics.

1.2 Basic idea of our proposal

Our proposal for non-destructive measurement relies on cross-phase modulation between a strong probe pulse, which is stored in a medium, and a weak detuned signal, which passes without attenuation through the medium. The probe is stored in an impurity-doped crystal using an approach based on atomic frequency combs [31], and the phase shift is due to the AC Stark shift of the relevant atomic transition caused by the propagating signal.

Our chosen medium for a proof-of-principle demonstration of our proposal is a rare-earth-ion (REI) doped crystal. As we will discuss in more detail in Chapter. 4, the $4f^n \rightarrow 4f^n$ inner-shell transitions of REIs show some very interesting properties. Due to shielding by the outer lying $5s$ and $5p$ electrons, these transitions are well isolated from the environment and are hence less prone to decoherence mechanisms. For instance, a coherence time of more than six hours has been reported for the ground state hyperfine levels [32]. These properties make REI doped crystals a very promising candidate for quantum information processing tasks. Already, there has been a lot of work that demonstrates the suitability of this technology platform for quantum photonics

[33, 34, 35, 36, 37, 38, 39].

In Chapter. 2, we will give a brief introduction to the equations governing light-matter interaction. In Chapter. 3, we will discuss a short theoretical description of our scheme. Following this, in Chapter. 4, we will give a detailed description of the proof-of-principle experiment using intense coherent pulses and an impurity-doped crystal that confirms the predictions of our theory. Finally, in Chapter. 5, we will discuss how our proposal can be implemented at the single-photon level.

1.3 Author contributions

The theory for the work presented in this thesis was done by Dr. Khabat Heshami and Prof. Christoph Simon. I was a part of the experimental team along with Dr. Neil Sinclair, Dr. Daniel Oblak and Prof. Wolfgang Tittel. I contributed to setting up and running the experiment, analyzing the data and writing the manuscript.

Chapter 2

Light-matter interaction

The experiments described in this thesis involve interaction between light and rare-earth-ions (REIs). Thus, a description of how this interaction works is imperative to understand the experiments outlined in this thesis. However, an exhaustive description of light-matter interaction is not necessary to understand the concepts presented in this thesis. For this reason, various approximations are made to arrive at a simpler yet useful description of this interaction. Two such approximations that are often made are to (a) treat light as a classical coherent electromagnetic field that is monochromatic (e.g. light from a laser), and (b) treat the atom as a two-level system whose transition frequency is almost the same as the frequency of the optical field [40].

We begin by describing the dynamics of such a two-level atom, which is a system with only two eigenstates. The dynamics of such a two-level atomic system in the presence of an applied laser field are similar to that of a spin-one-half particle in a magnetic field that were derived by Bloch, and are hence called the optical Bloch equations. We will discuss the set of Bloch equations in Section 2.1. In Section 2.2, we describe the dynamics of an electromagnetic field in a polarizing medium using Maxwell's equations. Since a polarizing medium is composed of an ensemble of two-level atoms, we then combine these two sets of equations to get what is referred to as the Maxwell-Bloch equations, which describe the dynamics of the combined light-atom system.

2.1 Bloch equations

Following the approach of any standard quantum optics textbook (see Chapter 2 of [40]), we begin with the total Hamiltonian $\hat{H}_t$ of a two-level atom in an electromagnetic field, which can be written as

$$\hat{H}_t = \hat{H}_A + \hat{\mathbf{d}} \cdot \hat{\mathbf{E}}, \tag{2.1}$$

where $\hat{H_A}$ is the Hamiltonian of the free atom and $\hat{\mathbf{d}} \cdot \hat{\mathbf{E}}$ describes the interaction Hamiltonian $\hat{H_{int}}$ which determines the coupling between the dipole moment operator $\hat{\mathbf{d}}$ of the atom with the electric field $\hat{\mathbf{E}}$. The Hamiltonian of a free atom can be written in terms of Pauli matrices as

$$\hat{H_A} = \frac{1}{2}(E_e + E_g)\hat{I} + \frac{1}{2}(E_e - E_g)\hat{\sigma_z}, \tag{2.2}$$

where E_e and E_g are the eigenvalues of the ground and excited energy eigenstates respectively. After defining $1/2(E_e + E_g)$ as the zero of energy, the expression for H_A becomes

$$\hat{H_A} = \frac{1}{2}\hbar\omega_0\hat{\sigma_z}, \tag{2.3}$$

where $\omega_0 = (E_e - E_g)/\hbar$. Notice that $\hat{H_A}$ only has diagonal elements as it is written in the basis formed by the energy eigenstates. The dipole moment operator $\hat{\mathbf{d}}$ for an atom can be written in the dipole approximation as $\hat{\mathbf{d}} = -e\hat{\mathbf{r}}$, where $\mathbf{r}$ is the operator for position. In terms of the Pauli matrices, $\hat{\mathbf{d}}$ has the form

$$\hat{\mathbf{d}} = \vec{d}\hat{\sigma_x}, \tag{2.4}$$

where $\vec{d}$ is a vector. Note that $\hat{\mathbf{d}}$ only has off-diagonal elements as free-atoms posses inversion symmetry and hence $\langle g|\hat{\mathbf{d}}|g\rangle = 0$ and $\langle e|\hat{\mathbf{d}}|e\rangle = 0$. However, if these atoms are trapped inside a solid, the solid-state environment may break this symmetry and as a result the atoms may also have a permanent dipole moment. The interaction Hamiltonian $\hat{H_{int}}$ can then be written as

$$\hat{H_{int}} = (\vec{d} \cdot \hat{\mathbf{E}})\hat{\sigma_x}. \tag{2.5}$$

We can now describe the evolution of the light-matter system in terms of the evolution of these Pauli matrices. The evolution of the Pauli matrices can be described using Heisenberg's equations as

$$i\hbar\dot{\hat{\sigma}_i} = [\hat{\sigma_i}, H_t], \tag{2.6}$$

where $\dot{\hat{\sigma}}_i$ refers to the time derivative of $\hat{\sigma}_i$. This leads to the following set of equations

$$\begin{aligned} \dot{\hat{\sigma}}_x &= -\omega_0 \hat{\sigma}_y, \\ \dot{\hat{\sigma}}_y &= \omega_0 \hat{\sigma}_x + \frac{2}{\hbar}[\vec{d}\cdot\hat{\mathbf{E}}]\hat{\sigma}_z, \\ \dot{\hat{\sigma}}_z &= \frac{-2}{\hbar}[\vec{d}\cdot\hat{\mathbf{E}}]\hat{\sigma}_y. \end{aligned} \tag{2.7}$$

So far, we have treated all variables associated with the atom and the optical field as operators. However, in cases where quantum correlations between the atom and the optical field can be ignored, replacing the operators with their expectation values leads to a set of simpler equations that are very useful. This also means that the expectation values of products of operators can now be factored into products of expectation values of individual operators, i.e. $\langle\hat{\sigma}_i\hat{\sigma}_j\rangle = \langle\hat{\sigma}_i\rangle\langle\hat{\sigma}_j\rangle$. Also, the electric field operator $\hat{\mathbf{E}}$ can now be replaced by its expectation value $\vec{E} = \langle\hat{\mathbf{E}}\rangle$. Writing $\vec{d} = d\vec{\mu}_d$, where $\vec{\mu}_d$ is a unit vector, we have

$$\frac{2}{\hbar}\vec{d}\cdot\vec{E} = \frac{2}{\hbar}d(\vec{\mu}_d\cdot\vec{E}) = \kappa E, \tag{2.8}$$

where $\kappa = \frac{2}{\hbar}d$ and E is the projection of $\vec{E}$ along the direction of $\vec{\mu}_d$. The following set of equations now follow from Eq. 2.7

$$\begin{aligned} \dot{s_x} &= -\omega_0 s_y, \\ \dot{s_y} &= \omega_0 s_x + \kappa E s_z, \\ \dot{s_z} &= \kappa E s_y, \end{aligned} \tag{2.9}$$

where $s_i = \langle\hat{\sigma}_i\rangle$. The electromagnetic field in such a semi-classical treatment is written as a monochromatic field with an envelope function $\mathscr{E}(t,z)$

$$E = \mathscr{E}(t,z)e^{-i\omega t} + c.c, \tag{2.10}$$

where $c.c$ is the complex conjugate of the preceding term of the equation. To reduce the number of rapidly changing variables, we invoke the rotating wave approximation (RWA). This involves: (i) ignoring all the terms that are rotating fast enough such that their cumulative effect on the relevant

time-scales (given by ω) is very small, followed by (ii) changing the coordinate reference frame to one that is rotating at a frequency of ω. Assumption (i) gives us the following set of equations

$$\begin{aligned} \dot{s_x} &= -\omega_0 s_y - \kappa \mathscr{E} s_z \sin(\omega t), \\ \dot{s_y} &= \omega_0 s_x + \kappa \mathscr{E} s_z \cos(\omega t), \\ \dot{s_z} &= -\kappa \mathscr{E} (s_y \cos(\omega t) - s_x \sin(\omega t)). \end{aligned} \tag{2.11}$$

We can now move into the rotating frame of reference by introducing the appropriate transformation matrix given by

$$\begin{bmatrix} u \\ v \\ w \end{bmatrix} = \begin{bmatrix} \cos(\omega t) & \sin(\omega t) & 0 \\ -\sin(\omega t) & \cos(\omega t) & 0 \\ 0 & 0 & 1 \end{bmatrix} \begin{bmatrix} s_x \\ s_y \\ s_z \end{bmatrix} \tag{2.12}$$

The equations governing the evolution of these new variables can now be written as

$$\begin{aligned} \dot{u} &= -\Delta v, \\ \dot{v} &= \Delta u + \kappa E w, \\ \dot{w} &= -\kappa E v, \end{aligned} \tag{2.13}$$

where $\Delta = \omega_0 - \omega$. The new variables u, v and w are called Bloch variables. Eq. 2.13 can be written more compactly as

$$\dot{\vec{\rho}} = \vec{\Omega} \times \vec{\rho}, \tag{2.14}$$

where $\vec{\rho}$ is a column vector with elements (u, v, w), which is called the Bloch vector, and $\vec{\Omega}$ is a colum vector with elements $(-\kappa \mathscr{E}, 0, \omega_0 - \omega)$. We can see from this equation that when a two-level system is driven, the Bloch vector rotates around the vector Ω with a frequency given by $|\Omega|$, which is referred to as the Rabi frequency.

2.2 Maxwell-Bloch equations

Maxwell's equations describe the dynamics of an electromagnetic field. When propagating through a homogeneous non-magnetic dielectric medium that features no free charges or currents, we ob-

tain the following wave equation (see Chapter 1 of [40])

$$(\frac{\partial^2}{\partial z^2} - \frac{1}{c^2}\frac{\partial^2}{\partial t^2})E(t,z) = \frac{1}{\varepsilon_0 c^2}\frac{\partial^2}{\partial t^2}P(t,z), \tag{2.15}$$

where P is the polarization density, i.e. the dipole moment per unit volume. The polarization density P can be written in terms of the electric field E as

$$P = \varepsilon_0(\chi^{(1)}E + \chi^{(2)}E^2 + +\chi^{(3)}E^3 + \cdots), \tag{2.16}$$

where χ^i is the ith order electric susceptibility of the medium. In the low excitation regime, the response is linear. So the polarization density P can be approximated as $P = \varepsilon_0\chi^{(1)}E$. Using Eq. 2.10, the polarization takes the form

$$P = \mathscr{P}(t,z)e^{-i\omega t} + c.c. \tag{2.17}$$

To derive solutions to Eq. 2.15 using Eqs. 2.10 and 2.17, we make the following two approximations: (i) the spatial extent of the envelopes $\mathscr{E}$ and $\mathscr{P}$ evolve much slower than the wave vector k, i.e. $\frac{\partial \mathscr{E}}{\partial z} \ll k\mathscr{E}$ and $\frac{\partial \mathscr{P}}{\partial z} \ll k\mathscr{P}$, and (ii) the temporal extent of the envelopes $\mathscr{E}$ and $\mathscr{P}$ evolve much slower than the frequency of the field, i.e. $\frac{\partial \mathscr{E}}{\partial t} \ll \omega\mathscr{E}$ and $\frac{\partial \mathscr{P}}{\partial t} \ll \omega\mathscr{P}$. Note that (i) and (ii) are called the slowly varying envelope approximation (SVEA). This simplifies Eq.2.15 to

$$(\frac{\partial}{\partial z} + \frac{n}{c}\frac{\partial}{\partial t})\mathscr{E} = \frac{ik_0}{2\varepsilon_0 n}\mathscr{P}, \tag{2.18}$$

where k_0 is the wave-vector of the electromagnetic field in vacuum, ε_0 is the permittivity of vacuum and n is the refractive index of the material. The above equations are written for an ensemble of two-level atomic systems with the same transition frequency. However, most media used in practice consist of many classes of atoms, each of which has a different absorption frequency. The absorption profile for such a medium can be described using the distribution function $g(\Delta)$, which satisfies

$$\int_{-\infty}^{\infty} g(\Delta)d\Delta = 1. \tag{2.19}$$

The polarization for one such class of atoms can be written as $\vec{P}(z,t) = Nd\langle\sigma_x\rangle$, where the dipole moment d is defined as in Eq. 2.4. For an inhomogeneously broadened medium, $\vec{P}$ can be written as

$$\vec{P}(z,t) = Nd\int_{-\infty}^{\infty} d\Delta\, g(\Delta) Re\{u(z,t,\Delta) + iv(z,t,\Delta)\}, \tag{2.20}$$

where $\langle\sigma_x\rangle = s_x$ is written in terms of the Bloch vectors u and v according to Eq. 2.12. Combining Eq. 2.20 with Eq. 2.18, we get what is called the Maxwell-Bloch equation

$$(\frac{\partial}{\partial z} + \frac{n}{c}\frac{\partial}{\partial t})\mathscr{E} = \frac{ik_0 Nd}{2\varepsilon_0}\int_{-\infty}^{\infty} d\Delta\, g(\Delta) Re\{u(z,t,\Delta) + iv(z,t,\Delta)\}. \tag{2.21}$$

These equations relate the dynamics of a two-level system with that of the electromagnetic field. They will hence form a common starting point to develop the theoretical models that are presented in this thesis.

Chapter 3

Theoretical proposal

This chapter describes our proposal for non-destructive detection of photonic qubits. The basic principle of our scheme is illustrated in Fig. 3.1 and Fig. 3.2. It is based on cross-phase modulation of a strong probe pulse that is stored in an inhomogeneously broadened medium using the atomic frequency comb (AFC) protocol [31] by a weak signal. In this chapter, we first theoretically describe the storage of the probe following the approach that was introduced in the previous chapter. This is followed by a quantum mechanical treatment of the signal propagation, which also gives us the cross-phase modulation it induces. Finally, we include the effects of loss on the signal.

3.1 Storage of probe

The first step in our protocol involves the storage of a classical probe pulse. For an inhomogeneously broadened medium with a spatial extent, the total Hamiltonian can be written as

$$\hat{H} = \hat{H}_0 + \hat{H}_{\text{int}}, \tag{3.1}$$

where

$$\hat{H}_0 = \sum_{j=1}^{N} \hbar\omega_{\text{ge}}^{j} \hat{\sigma}_{\text{ee}}^{j}. \tag{3.2}$$

Here, $\hbar\omega_{\text{ge}}^{j}$ denotes the transition energy of atom j between ground and excited states ($|g\rangle$ and $|e\rangle$). Note that the eigenvalue associated with the energy eigenstate $|g\rangle$ has been defined as zero for mathematical simplicity. Also,

$$\hat{H}_{\text{int}} = -\hbar \sum_{j=1}^{N} \left(\Omega(z,t) \hat{\sigma}_{\text{eg}}^{j} e^{-i\omega_p (t - z_j/c)} + H.c. \right). \tag{3.3}$$

where ω_p is the control frequency of the probe field and H.c. is the Hermitian conjugate of the first term inside the summation. $\Omega(z,t) = \frac{\mu_{\text{eg}} \mathscr{E}_p(z,t)}{2\hbar}$ is the Rabi frequency associated with the probe field,

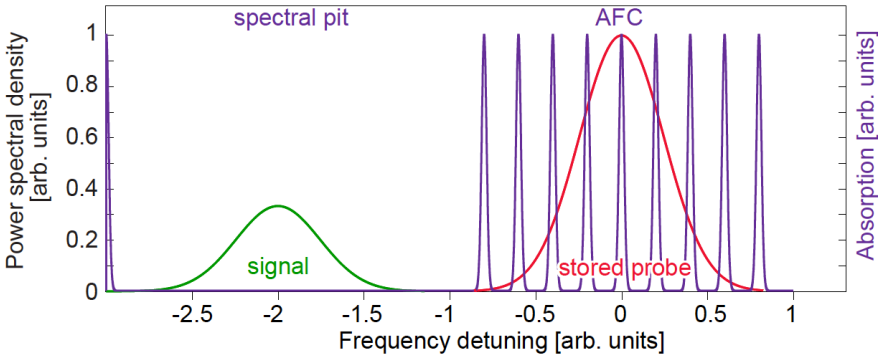

Figure 3.1: Protocol for non-destructive detection of photonic time-bin qubits. A macroscopic probe pulse is stored in an atomic frequency comb (AFC). The signal — a photonic time-bin qubit — propagates through a detuned transparency window and shifts the resonance frequency of the atoms that constitute the AFC via the AC Stark effect. This results in a phase shift of the re-emitted probe. A spectral representation of our protocol is shown here. Figure taken from [1].

and $\mu_{\mathrm{eg}} = \langle e|\hat{\mathbf{d}}\cdot\boldsymbol{\varepsilon}_p|g\rangle$ is the transition dipole moment, where $\mathscr{E}_p$ is the slowly varying component of the probe field $\mathbf{E}_p(z,t) = \boldsymbol{\varepsilon}_p\mathscr{E}_p(t-z/c)\cos(\omega_p(t-z/c))$ with polarization unit vector of $\boldsymbol{\varepsilon}_p$. The atomic coherence and population for atom j are defined by $\hat{\sigma}^j_{\nu\nu'} = |\nu\rangle^j\langle\nu'|$, where $\nu,\nu' = \{\mathrm{g},\mathrm{e}\}$.

We can now define collective atomic coherence and population operators for all atoms in a slice of the medium at (longitudinal) position z and relative resonance frequency δ as follows,

$$\hat{\sigma}_{\mathrm{gg}}(z,t;\delta) = \frac{1}{N_z(\delta)}\sum_{i=1}^{N_z(\delta)}\hat{\sigma}^i_{\mathrm{gg}}(t;\delta), \tag{3.4}$$

$$\hat{\sigma}_{\mathrm{ee}}(z,t;\delta) = \frac{1}{N_z(\delta)}\sum_{i=1}^{N_z(\delta)}\hat{\sigma}^i_{\mathrm{ee}}(t;\delta), \tag{3.5}$$

and

$$\hat{\sigma}_{\mathrm{eg}}(z,t;\delta) = \frac{1}{N_z(\delta)}\sum_{i=1}^{N_z(\delta)}\hat{\sigma}^i_{\mathrm{eg}}(t;\delta)e^{-i\omega_p(t-z_i/c)}. \tag{3.6}$$

Here, $\omega_0 = \omega_p$ is the central frequency of the inhomogeneously-broadened atomic ensemble and δ denotes the detuning of different resonances in the ensemble with respect to ω_p, where we assume that the number of atoms in mode δ at z, $N_z(\delta)$, is much larger than 1.

Using the Heisenberg equation (Eq. 2.6), one can find the following dynamical equations for

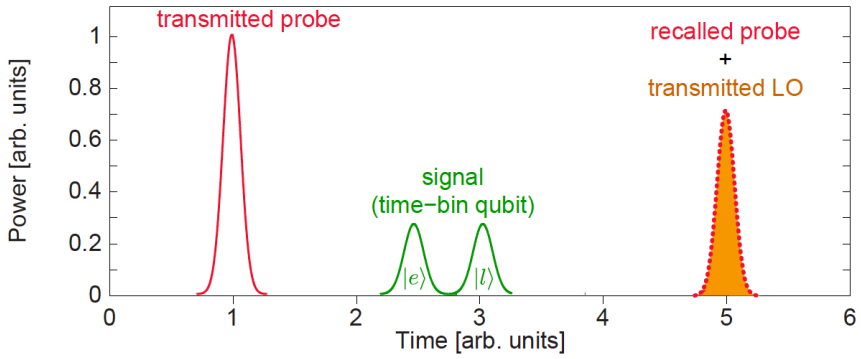

Figure 3.2: A temporal representation of our protocol is shown here. The time-bin qubit states $|e\rangle$ and $|l\rangle$ refer to early and late temporal modes, respectively. Figure taken from [1].

the collective operators

$$\dot{\hat{\sigma}}_{gg}(z,t;\delta) = i\Omega^*(z,t)\hat{\sigma}_{ge}(z,t;\delta) - i\Omega(z,t)\hat{\sigma}_{eg}(z,t;\delta), \tag{3.7}$$

$$\dot{\hat{\sigma}}_{ee}(z,t;\delta) = i\Omega(z,t)\hat{\sigma}_{eg}(z,t;\delta) - i\Omega^*(z,t)\hat{\sigma}_{ge}(z,t;\delta), \tag{3.8}$$

and

$$\dot{\hat{\sigma}}_{eg}(z,t;\delta) = i(\omega_0+\delta-\omega_p)\hat{\sigma}_{eg}(z,t;\delta) + i\Omega^*(z,t)\hat{\sigma}_{ee}(z,t;\delta) - i\Omega^*(z,t)\hat{\sigma}_{gg}(z,t;\delta). \tag{3.9}$$

The propagation of the probe field can be derived using Maxwell's equations (Eq. 2.18) as

$$\left(\partial_z + \frac{n}{c}\partial_t\right)\mathscr{E}_p(z,t) = \frac{i\mu_0\omega_p^2}{2k_p}\langle\hat{\mathscr{P}}_{tot}\rangle, \tag{3.10}$$

where $\mathscr{E}_p(z,t)$ is the slowly varying envelope of the probe field, $k_p = \frac{n\omega_p}{c}$ and $\langle\hat{\mathscr{P}}_{tot}\rangle$ denotes the expectation value of

$$\hat{\mathscr{P}}_{tot} = \sum_{\delta}\langle g|\hat{\mathbf{d}}\cdot\boldsymbol{\varepsilon}_p|e\rangle\frac{N(\delta)}{V}\hat{\sigma}_{ge}(z,t;\delta). \tag{3.11}$$

Eqs. 3.7, 3.8 and 3.9 along with Eqs. 3.10 and 3.11 allow us to describe the dynamics of the atoms due to the probe field for times $t < T_1$ and $t > T_2$, where T_1 and T_2 determine the expected time window for the propagating time-bin signal field. Between storage and retrieval of the probe ($T_1 < t < T_2$) the evolution is perturbed by the signal field (see below).

For optimum phase sensitivity the number of absorbed photons N_p should be of order $N/2$, where N is the total number of atoms in the AFC. In this case the number of atoms remaining in the ground state N_g is equal to N_p, $N_g = N_p = N/2$.

3.2 Cross-phase modulation due to signal

In this section, we provide the theoretical model for the interaction between the signal and the atoms. For large detunings, where Δ is larger than the signal bandwidth, we derive an effective interaction Hamiltonian that will be used to find the probe phase shift with respect to the number of photons in the signal field. Using the collective atomic operators that are defined in Eqs. 3.4, 3.5 and 3.6, we can write the following for the collective atomic polarization (see Appendix A for a detailed derivation)

$$\hat{\sigma}_{\mathrm{eg}}(z, t = T_2; \delta) = e^{i\delta t} e^{i\hat{\Phi}} \hat{\sigma}_{\mathrm{eg}}(z, t = T_1; \delta), \tag{3.12}$$

where

$$\hat{\Phi} = \int_{T_1}^{T_2} dt' \frac{2g^2}{\Delta} \left(\hat{\mathscr{E}}_s(z,t') \hat{\mathscr{E}}_s^{\dagger}(z,t') + H.c. \right). \tag{3.13}$$

Note that, for the abve case, we use the quantum-mechanical Hamiltonian for the interaction between the signal and the atoms, which is different from the semi-classical approach described in Chapter. 2. A frequency offset such as the one shown in Equation 3.12 leads to a phase factor for the re-emitted probe field (see [31]). Therefore, phase modulations due to the presence of the signal will be imprinted on the retrieved echo. In addition, the total phase depends only on the total energy in the signal field and does not reveal any information about the temporal distribution of the signal field.

3.3 Phase-shift per photon

Given 3.13, the total phase shift for a single-photon signal propagating in the waveguide and interacting off-resonantly with the atomic polarization is given by

$$\phi = \frac{2g^2}{\Delta}\tau_s \tag{3.14}$$

where $\tau_s = L/c$ is the duration of the signal in vacuum and the single photon coupling rate is given by $g = \mu_{\mathrm{eg}}\sqrt{\frac{\omega_s}{2\hbar\varepsilon V}}$. The spontaneous emission rate of a two-level system is related to its transition dipole moment according to $\gamma = \frac{\mu_{\mathrm{eg}}^2\omega_0^3}{\pi\varepsilon\hbar c^3}$ [41]. Assuming that $\lambda_s \approx \lambda_0$ we can find the phase shift due to a single photon as

$$\phi = \frac{2g^2}{\Delta}\tau_s = \frac{1}{4\pi}\frac{\lambda_0^2}{n^2 A}\frac{\gamma}{\Delta}, \tag{3.15}$$

where A is the transverse mode area of the interaction, and λ_0 is the wavelength associated with the corresponding atomic transition in vacuum.

3.4 Signal loss

In this section, we analyse the signal loss due to its off-resonant interaction with the atoms in the AFC. In order to find a simplified description for off-resonant absorption loss, we assume that the signal detuning is larger than the inhomogeneous bandwidth of the ensemble. This also guarantees that Δ is much larger than the spontaneous emission rate, γ.

To analyse the signal loss, we take the Fourier transform of the Maxwell-Bloch equations. As a result, the frequency domain representation of the output signal is given by

$$\tilde{\mathcal{E}}_s(z,\omega)|_{z=L} = e^{ik_s\chi(\omega)L}\tilde{\mathcal{E}}_s(z=0,\omega), \tag{3.16}$$

where $\chi(\omega)$ is the susceptibility of the medium. The imaginary part of $\chi(\omega)$ determines the loss, which can be simplified by assuming $\Delta \gg \Gamma$, where $-\Gamma/2 < \delta < \Gamma/2$. In addition, the loss is expected to be uniform over the signal field spectrum when its bandwidth is much smaller than the

detuning ($\Delta \gg 1/\tau_s$). This results in a simple expression for the imaginary part of the response function $\chi(\omega)$, which is given by (see Appendix A for a detailed derivation)

$$\text{Imag}(\chi(0)) = \frac{1}{k_s}\frac{1}{16\pi}\frac{N_g\lambda_0^2\gamma^2}{n^2V\Delta^2}. \tag{3.17}$$

Therefore, the intensity loss for the signal field can be derived from

$$|\mathscr{E}(L,\omega)|^2 = e^{-\zeta L}|\mathscr{E}(0,\omega)|^2, \tag{3.18}$$

where

$$\zeta L = \frac{1}{8\pi}\frac{N_g\lambda_0^2}{n^2A}\frac{\gamma^2}{\Delta^2}. \tag{3.19}$$

To minimize noise for the signal, it is desirable not to have significant population in the excited state when the signal propagates through the medium. This can be achieved by transferring the excited state population to another ground state after the probe has been absorbed. The phase shift on the probe in this case would be smaller by a factor of 2 as this second ground state will be unaffected by the AC Stark shift due to the signal.

3.5 Requirements for single-photon sensitivity

Single photon sensitivity requires $\sqrt{\eta N_p}\phi > 1$, with ϕ given by Equation (3.15) with an additional factor $1/2$ assuming that the excited state population is transferred to another ground state to minimize loss and noise. Here η is the retrieval efficiency of the probe field in the AFC [31],

$$\eta = (1-e^{-d/F})^2 e^{-\frac{\pi^2}{2\ln 2F^2}}, \tag{3.20}$$

where d and $F = \Delta_m/\gamma$ are optical depth and finesse of the AFC, respectively. Assuming $N_p = N_g$, as discussed above, this puts a lower bound on the number of atoms in g,

$$N_g > \frac{1}{\eta\phi^2} = \frac{1}{\eta}\left(\frac{8\pi n^2 A\Delta}{\lambda_0^2\gamma}\right)^2, \tag{3.21}$$

and hence a lower bound on the loss experienced by the signal:

$$\zeta L = \frac{N_g\lambda_0^2\gamma^2}{8\pi n^2 A\Delta^2} > \frac{8\pi n^2 A}{\eta\lambda_0^2}. \tag{3.22}$$

Even for very small cross sections of order λ_0^2/n^2, this loss is $8\pi/\eta \gg 1$, which is too high for a nondestructive measurement. A similar limitation has also been pointed out for generating giant Kerr nonlinearity based on EIT [42].

3.5.1 Multi-pass arrangement

This problem can be overcome by using a multi-pass arrangement, where m is the number of passes the signal makes through the medium. In this case the phase shift ϕ in Equation (3.15) and the relation for the loss ζL are both multiplied by m. However, the lower bound on N_g of Equation (3.21) that originates from the single photon sensitivity requirement scales as $1/\phi_{\text{tot}}^2$, where $\phi_{\text{tot}} = m\phi$. Therefore, the lower bound on N_g of Equation (3.21) is multiplied by $\frac{1}{m^2}$, which finally leads to a modified bound on the total loss,

$$m\zeta L > \frac{8\pi n^2 A}{m\eta\lambda_0^2}, \tag{3.23}$$

which can be much less than one for sufficiently many passes. Requiring small total signal loss $m\zeta L \lesssim 0.1$, Equation (3.23) gives a condition on m,

$$m > 80\pi/\eta, \tag{3.24}$$

where we have assumed $A = \lambda_0^2/n^2$.

Implementing $m \gg 1$ in practice requires low-loss switches. However, an analogous effect can also be achieved by using a cavity. The main difference is that a cavity enhances the signal field rather than the interaction time, which reduces the requirements on the storage time for the probe compared to a multi-pass scenario. Here we focus on the multi-pass case for simplicity.

For a small A, and for an AFC where each tooth corresponds to one radiatively broadened line, the optical depth per atom for each absorption line is $\lambda^2/n^2 A \approx 1$. This leads to number of atoms in each AFC tooth to be equal to the optical depth and therefore having the total number of atoms in the inhomogeneously broadened ensemble N as $N = n_t d$, where n_t is the number of teeth in the comb. This leads to another condition that follows from Equation (3.21), which in the multi-pass

case, can be rewritten as

$$d > \frac{128\pi^2\Delta^2}{n_t\gamma^2 m^2\eta}, \tag{3.25}$$

where in deriving Equation (3.25) we have again assumed $N_g = N/2$. Equation (3.25) yields a condition on the number of passes,

$$m > \frac{8\sqrt{2}\pi\Delta}{\sqrt{n_t\eta d\gamma}}. \tag{3.26}$$

We now rewrite the detuning $\Delta = f n_t F\gamma$, where $F = \Delta_m/\gamma$ is the finesse of the AFC and f is a factor greater than one that assures that the signal is sufficiently far detuned from the AFC (whose total width is $n_t F\gamma$). This yields

$$m > 8\sqrt{2}\pi f F\sqrt{\frac{n_t}{d\eta}}. \tag{3.27}$$

Eq. (3.26) also yields a condition on the number of passes as a function of the desired signal bandwidth B. For B expressed in Hz one has $B = \Delta/(2\pi f)$, where the factor f again ensures that the signal is off-resonant. This gives

$$m > \frac{16\sqrt{2}\pi^2 fB}{\sqrt{n_t\eta d\gamma}} \tag{3.28}$$

For our material system (Tm ions in Lithium Niobate, which have γ of approximately 9 kHz) all the above conditions are satisfied, for example, by setting $f = 3$, $d = 30$ as achieved in Ref. [**?**], $B = 500$ kHz, $F = 3.2$, $n_t = 110$ and $m = 930$.

Chapter 4

Proof-of-principle demonstration

We perform a proof-of-principle demonstration of our proposal using a Thulium (Tm) doped $LiNbO_3$ waveguide. Tm:$LiNbO_3$ is a crystal that has been employed to demonstrate various quantum information processing tasks [37, 39]. In this chapter, we will first discuss some of the spectroscopic properties of REI doped crystals with emphasis on the specific properties of a Tm:$LiNbO_3$ waveguide followed by a detailed description of our experimental demonstration.

4.1 Rare earth elements

The term rare-earth element refers to the set of fifteen lanthanides in the sixth period of the periodic table along with scandium and yttrium. When these rare-earth elements are doped in a solid-state material, they form trivalent ions whose electronic configuration is of the form $[Xe]4f^n$, where n is zero for lanthanum and increases according to increasing atomic number. These REIs feature interesting properties with respect to $4f^n \rightarrow 4f^n$ inner-shell transitions. The $4f^n \rightarrow 4f^n$ transitions, which are dipole-forbidden in a free-REI, become weakly allowed when REIs are doped into crystals due to a mixing of energy levels in the presence of the electrostatic field of the crystal. The resulting weak light-matter coupling results in these levels having slow relaxation rates. More importantly, due to shielding from the outer lying $5s$ and $5p$ electrons, these transitions are somewhat isolated from the environment and are consequently less prone to decoherence. When cooled to cryogenic temperatures, these transitions exhibit excellent coherence properties [43], which make them very promising candidates for storing and processing quantum information.

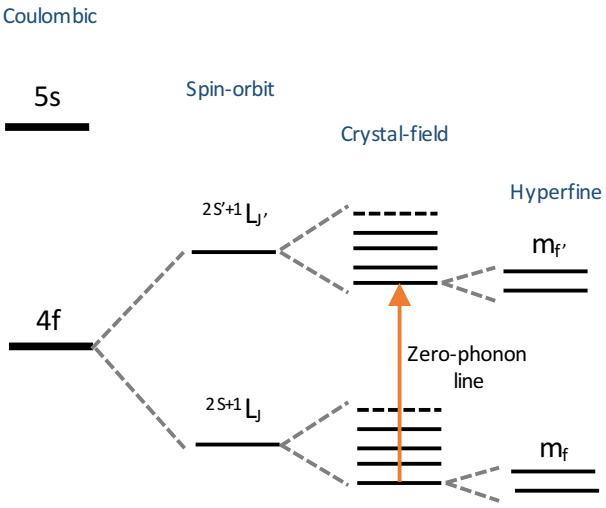

Figure 4.1: Typical energy level structure of triply-ionized REIs doped into crystals. Also represented are the energy corrections due to crystal-field interaction.

4.2 Energy level structure and lifetimes of rare-earth-ions

Compared to other ions, the energy level structure of a REI doped into a crystal is complex due its high atomic number and the perturbations introduced by the solid-state environment. The largest energy contribution to the energy level structure comes from the Coulombic interaction between the nucleus and the electron and the interaction between the orbital angular momentum of the electron and its spin, i.e. the spin-orbit coupling. The energy levels resulting from these interactions are represented using the following three quantum numbers: (i) total orbital angular momentum L, (ii) total spin angular momentum S and (iii) total angular momentum J. The energy levels are written as $^{2S+1}L_J$ (see Fig. 4.1).

When a REI is now placed in a crystalline environment, the next most significant contribution comes from the electrostatic fields that are present in the host crystal. These fields split each of these J-manifolds via Stark effect into $2J+1$ (for non-Kramer's ions) or $J+1/2$ (for Kramer's ions) so-called crystal-field or Stark levels. The energy separation between each of these Stark

levels within a J-manifold is typically of the order of hundreds of GHz [43].

4.2.1 Hyperfine and Zeeman levels

To map the energy level structure further, we consider the interaction of the nuclear magnetic moment with the magnetic field generated by the electron, which is called the hyperfine interaction, and with an external magnetic field (including both applied and from the crystal), which is called the Zeeman effect [43]. The energy levels resulting from the hyperfine interaction are represented using the quantum number F_l that describes the coupling between the total angular momentum of the electron J and the nuclear spin I. For ions with an odd number of electrons, which are called Kramer's ions, the hyperfine interaction results in electronic doublets. For non-Kramer's ions, the hyperfine interaction depends on the symmetry of the crystal into which the ion is doped. For sites with low symmetry, there is no first order hyperfine interaction and hence results in electronic singlets. However, for sites with high degree of symmetry, a non-zero angular momentum exists for the electron along the axis of symmetry and hence results in electronic doublets [43].

Thulium, which is a non-Kramer's ion with a nuclear spin of $I = \frac{1}{2}$, doped into a $LiNbO_3$ crystal experiences an environment with a C_3 symmetry around the c-axis of the crystal. This results in energy levels that are electronic singlets [41]. When an external magnetic field is applied, both the ground and the excited states split into two levels, which are represented as $m_s = +\frac{1}{2}, -\frac{1}{2}$.

4.2.2 Lifetimes

The lifetime of an excited level, which is referred to as T_1, is related to the rate of decay from it to any other level. For a REI doped into a crystal, this decay can happen via two mechanisms. In the first, the REI decays by spontaneously emitting a photon. This process is called a radiative process and this rate can be calculated (see [44]). The second mechanism pertains to emission in the form of thermal/vibrational energy, which are called phonons. As these processes don't involve photons, they are called non-radiative processes. While radiative processes are largely independent of temperature, non-radiative processes are not. Non-radiative processes are also typically much faster

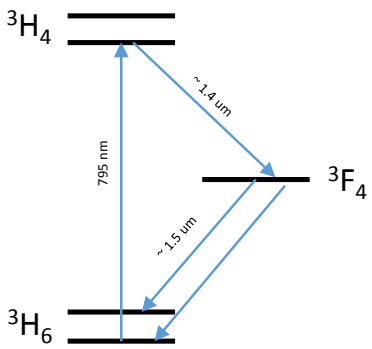

Figure 4.2: Simplified energy level structure of Tm ions showing the most relevant levels for work in this thesis. The ground state is $^3H_6$. The line at around 795 nm represents the transition from the lowest Stark level in the $^3H_6$ manifold to the lowest Stark level in the $^3H_4$ manifold.

when compared to radiative processes [43]. Even when REI doped crystals are cooled to cryogenic temperatures, the effect of phonons is significant for Stark levels within a given J-manifold. Hence, transitions between non-lowest Stark levels always involve phonons. The frequency separation between two different J-manifolds is however much larger than the maximally allowed frequency of phonons. As a result, there exist transitions between the lowest lying Stark levels that do not involve phonons. For this reason, when considering transitions between the ground and excited states, we will only consider transitions from the lowest lying Stark level in the ground state to the lowest lying Stark level in the excited state. This transition line is referred to as the 'zero phonon line' (see Fig. 4.2).

For Tm:$LiNbO_3$, we consider transitions between the lowest lying Stark level in the $^3H_6$ manifold to the lowest lying Stark level in $^3H_4$ manifold, as shown in Fig. 4.2. The lifetime of the $^3H_4$ level has been reported to be more than 100 μs [45, 41]. In our experiment, we also apply a magnetic field that results in both the ground and the excited states splitting into two nuclear zeeman levels. The lifetime of the ground state hyperfine level has been reported to be more than 2 hours [46].

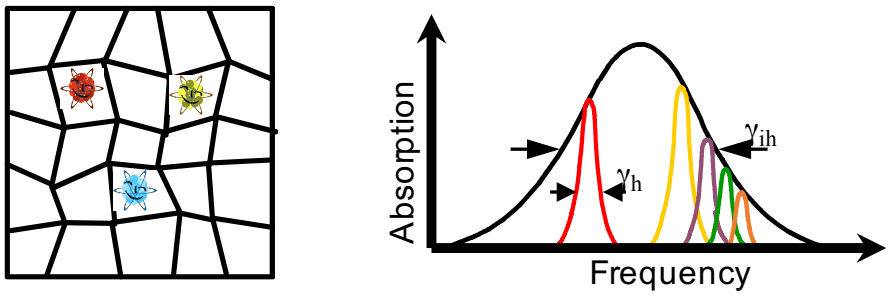

Figure 4.3: Inhomogeneous broadening. Imperfections in the crystal (illustrated on the left) result in the ions experiencing different environments in the crystal. This results in an inhomogeneous broadening γ_{ih} of lines in addition to homogeneous broadening γ_h (shown on right).

4.3 Linewidths

4.3.1 Homogeneous linewidth

The spectral lines associated with any transition of the atomic levels are broadened by various mechanisms and hence have a finite spectral width associated with them. When such line-broadening happens uniformly for all emitters in the system, it is referred to as homogeneous line-broadening, and the associated line-width is called homogeneous line-width. The homogeneous line-width is related to the coherence time T_2 through the following time-frequency Fourier transform:

$$\Gamma_h = \frac{1}{\pi T_2} \tag{4.1}$$

The coherence time of any level is theoretically bound by the the lifetime of that level, such that $T_2 \leq 2T_1$. In practice however, the observed coherence times are much shorter than the lifetime of the levels due to various decoherence processes. Predominant mechanisms that contribute to such decoherence are: (i) coupling of the energy levels to phonons, which leads to a reduced lifetime due to phonon-scattering, and (ii) spectral diffusion, which randomly varies the energy of the atomic levels that consequently broadens the line. All the experiments discussed in this thesis are

carried out at temperatures below 1 K, where linewidth broadening due to phonon-scattering can be neglected. So, the decoherence is dominated by spectral diffusion. Spectral diffusion results from time-dependent perturbations of the environment, such as the electric or magnetic field experienced by the REI. This predominantly happens via two mechanisms: (i) spin flips, which involves the flip of a nuclear spin in the vicinity of the REI, such as that of a host atom or another REI, and (ii) spin flip-flops, where there is an exchange of energy between two spins that are resonant with each other.

For the Tm:$LiNbO_3$ waveguide, coherence times for the $^3H_6 \rightarrow ^3 H_4$ transition have been reported to be over 1 μs at liquid helium temperatures [47, 45] and over 100 μs at temperatures below 1 K [46]. The latter corresponds to a homogeneous linewidth of less than 10 KHz.

4.3.2 Inhomogeneous broadening

REIs doped in crystals experience different local environments due to imperfections in the crystal lattice. As a result, the resonance frequency of each ion is slightly different. The absorption spectrum of an ensemble of REIs consists of the sum of homogeneously broadened lines that are each shifted inhomogeneously, as shown in Fig. 4.3. The inhomogeneous broadening depends on factors like the quality of crystal and the doping concentration, and can range from a few tens of MHz to several hundreds of GHz. This combination of narrow homogeneous linewidths and broad inhomogeneous linewidths allows for long-term storage of broadband light.

4.4 Experimental implementation of our protocol

4.4.1 Spectral tailoring using optical pumping

To use REI-doped crystals for quantum storage purposes, we need to spectrally tailor the inhomogeneous broadening to suit our applications. This is achieved by a process called as optical pumping where ions that absorb at a certain frequency for a given transition are pumped using optical pulses into a detuned and metastable level. This is illustrated in Fig. 4.4. Optical pulses

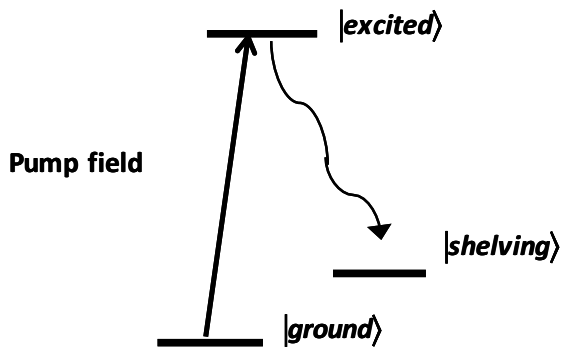

Figure 4.4: Optical pumping. Here the pump field puts ions that are in the ground state into the excited state from where they decay either back to the ground state or to some long-lived shelving level. Repeated pumping results in all ions in the shelving level.

excite ('pump') ions into an excited state that features a short lifetime compared to the metastable level. If this process is repeated for sufficient time all the ions that are being optically pumped end up in the metastable level, hence leaving no absorbers that feature a resonance frequency matching that of the pump pulse.

4.4.2 Tm:$LiNbO_3$ waveguide

Fabricating the Tm:$LiNbO_3$ waveguide (described in more detail in [45]) first involves in-diffusion of electron-beam evaporated and vacuum deposited layer of thulium into a commercially-available $LiNbO_3$ wafer. This is followed by in-diffusion of thin Ti stripes into the Tm doped $LiNbO_3$ surface, which forms waveguides. The waveguide is single-mode for TE and TM polarizations around 795 nm with a spatial-mode diameter of $\sim$12.5 μm.

This crystal is placed inside a cryostat that is cooled to below 1 K. Optical access is provided by single-mode optical fibres at the input and output, both of which are single-mode at the operational wavelength of 795 nm. The total coupling efficiency from the input fibre into the waveguide and then back into the output fibre is approximately 10%.

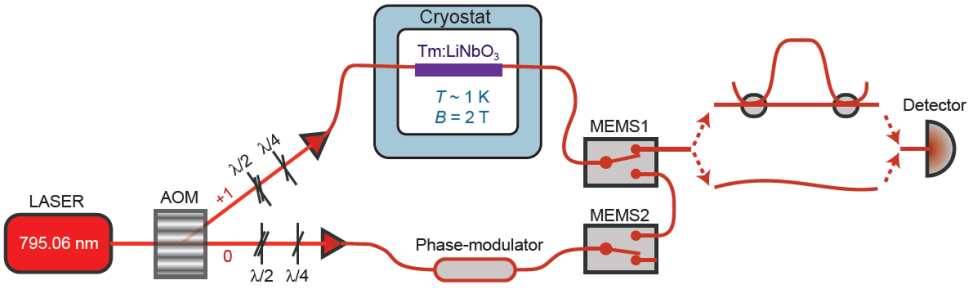

Figure 4.5: Experimental setup consisting of a continuous-wave laser at 795.06 nm, which is intensity and frequency modulated using an acousto-optic modulator (AOM). The diffracted first-order beam is coupled via a fibre into the Tm:$LiNbO_3$ waveguide, and wave-plates enable adjusting its polarization to maximize the interaction with Tm ions. The zeroth-order is frequency modulated using a phase-modulator to reinitialize the absorption spectrum after each experimental cycle. Figure taken from [1].

4.4.3 Experimental setup

Our experimental set-up, which is sketched in Fig. 4.5, consists of a continuous-wave laser at 795.06 nm, which is intensity and frequency modulated by driving an acousto-optic modulator (AOM) with appropriate radio-frequency (RF) signals. The bandwidth of the AOM is about 300 MHz with central frequency at 400 MHz. Driving the AOM with an RF signal generates periodic changes in the refractive index of the material constituting the AOM which in turn generates a diffraction pattern for the input light. The first-order of the diffracted beam, whose frequency with respect to the input beam depends on the frequency of the driving RF signal, will be used both for spectral tailoring as well as for creating the probe and signal pulses. Prior to being coupled into the waveguide, the light passes through a combination of wave-plates that enable adjusting the polarization of the light to maximize the interaction with Tm ions. The setup also consists of micro electro-mechanical switches (MEMS) at the output of the waveguide that allow for routing light into and out of different components of the setup depending on the type of measurement, i.e either directly to the detector or via an interferometer that assesses the change in the signal. The phase-modulator (PM) in the setup is used at the end of each experimental cycle to reinitialize the spectral absorption, as we will discuss in more detail below.

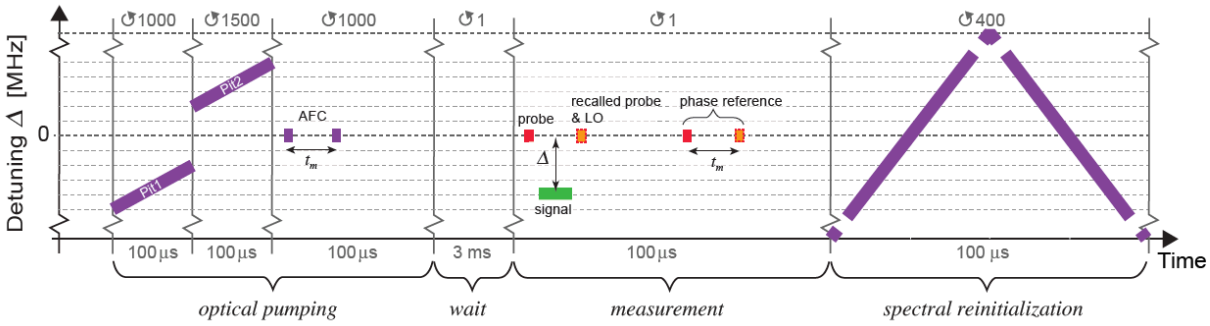

Figure 4.6: Timing sequence. Optical pumping involves repetitive spectral pit burning at negative (-150 to -50 MHz) and positive (50 to 150 MHz) detunings for at total of 250 ms, and AFC generation using many pulse-pairs for 100 ms. (Depicted is one repetition while the number following the circular arrow indicates the repetitions per task). Next, we wait for 3 ms to allow the excited atomic population to decay. This is followed by the measurement which involves storing the probe in the AFC, transmission of a detuned signal through a spectral pit, interferometric measurement of the recalled probe pulse with local oscillator (LO), and a phase reference measurement. Finally, we reinitialize the absorption line after every measurement using zeroth-order light from the AOM that is repetitively frequency-modulated over a 5-GHz range by a phase modulator. Figure taken from [1].

The first step in the experiment is creating the required spectral feature, which is discussed in detail below. This is followed by performing two types of measurements. The first involves: (i) storing the probe, (ii) sending the signal, and finally (iii) extracting the phase imprinted onto the recalled probe by performing an interferometric measurement with a local oscillator. The second involves sending the signal through an interferometer to assess changes in it.

4.4.4 Spectral tailoring

The metastable level used for optical pumping is another ground-state nuclear Zeeman level [41]. The splitting of the nuclear Zeeman level is $\sim$1.2 GHz/T, which results in a total splitting of $\sim$2.5 GHz in the applied magnetic field of 2 T. Optical pumping is achieved using the continuous-wave laser at 795.06 nm, which is frequency modulated by driving the AOM with RF signals. A suitable configuration of MEMS1 is used to block laser light from reaching the detector during this process. The required spectral feature is shown in Fig. 4.7, which includes an AFC that is

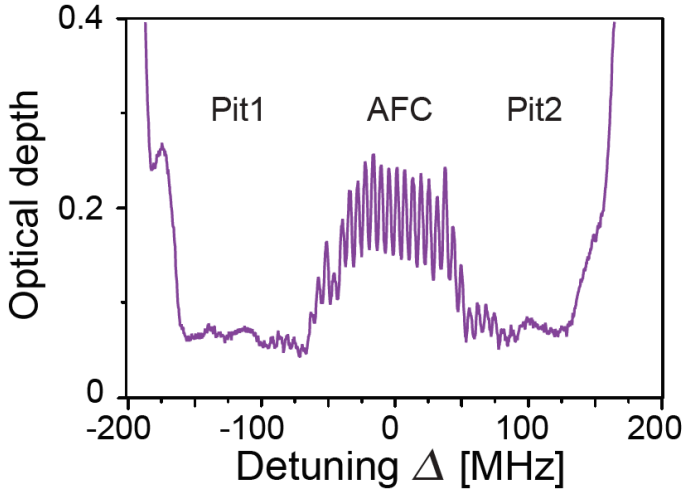

Figure 4.7: Spectral feature. A 100 MHz wide AFC with a tooth separation $\Delta_m/(2\pi)$ = 5.5 MHz (corresponding to a storage time of $t_m = 180$ ns) and a 100 MHz wide spectral pit on either side of the AFC. Figure taken from [1].

surrounded on both sides by transparent pits with almost no residual absorption. The sequence of frequency modulation used to create the required spectral feature is illustrated in Fig. 4.6.

We begin the spectral tailoring by sweeping the frequency of the laser light repeatedly over two 100 MHz wide regions - one at negative detuning from -150 to -50 MHz, and another at positive detuning from 50 to 150 MHz, for a total of 250 ms, as illustrated in Fig. 4.6. This generates spectral regions that are almost transparent with a very small remaining optical depth of around 0.07. They are irregular due to varying efficiency of the AOM with detuning. Next, we generate an AFC in-between the two pits from -50 MHz to +50 MHz by driving the AOM using pairs of pulses that are 10 ns wide and separated by 180 ns, for a total of 100 ms. This results in an AFC with a bandwidth of 100 MHz and a tooth separation of $\Delta_m/(2\pi) = 5.5$ MHz, which corresponds to a storage time of 180 ns. The tooth separation is chosen to match side-peaks at 11 MHz arising from the super-hyperfine interaction of thulium with niobium in the host crystal [46]. The teeth feature an optical depth of $\sim$0.1, and are sitting on a background with optical depth of $\sim$0.15, resulting in a recall efficiency for the probe of 0.2% [31]. After the optical pumping cycle is complete, we wait for 3 ms to allow the excited atomic population to decay before performing our measurement. The

measurements are done with strong laser pulses that modify the tailored spectral feature. Hence, we reinitialize the absorption line after every measurement using zeroth-order light from the AOM that is repetitively frequency-modulated over a 5-GHz range by a phase modulator (PM). A suitable configuration of the two MEMS switches (MEMS1 and MEMS2) is used to allow the zeroth-order light into the Tm-doped waveguide during this time.

The quality of our spectral feature — the background in the pits and the AFC, as well as the small optical depth of the AFC teeth — is currently limited by non-ideal spectral tailoring. It can be improved by using a laser with improved stability, and by optical pumping based on a burn-back method [35].

4.4.5 Cross-phase modulation using signal states encoded in strong pulses

Following the spectral tailoring, we first perform measurements with strong signal pulses to verify the phase shift on the probe predicted by the following equation that was derived in Chapter 3:

$$\phi = \frac{N_s}{4\pi}\frac{\lambda_0^2}{n^2 A}\frac{\gamma}{\Delta}, \tag{4.2}$$

where N_s is the number of photons in the signal pulse, λ_0 is the wavelength associated with the corresponding atomic transition in vacuum, A is the transverse mode area of the interaction, γ is the spontaneous decay rate from the excited state and Δ is the detuning of the signal from the central frequency of the probe, which is the same as the central frequency of the AFC. The parameters that we vary in this experiment are N_s and Δ. All the other parameters are determined by the properties of the Tm:$LiNbO_3$ waveguide.

The first measurement involves the following steps: (i) store the probe pulse in the AFC, (ii) send the signal through the transparent pits around the AFC, and finally (iii) extract the phase imprinted onto the recalled probe by performing an interferometric measurement with a local oscillator. We begin the measurement by generating a probe pulse of ~ 10 ns duration whose spectrum matches that of the AFC. A part of the pulse is transmitted through the waveguide and a part of it is stored in the thulium ions that form the AFC. We then send a signal in a single temporal mode

of 130 ns duration. After the storage time t_m of the AFC the probe pulse is re-emitted from the waveguide. The phase change imprinted on the recalled probe due to interaction with the signal is assessed via an interferometric measurement of the recalled probe pulse with a transmitted local oscillator (LO) in the same spatial, temporal and spectral mode, and featuring the same intensity. First, by varying the phase of the LO in the absence of a signal, we calibrate the interference visibility to 89.7%. Next, to ensure maximum measurement sensitivity, we set the phase difference between the LO and the recalled probe (still without a signal) to $\pi/2$. Taking the calibration into account, this allows us in the actual measurement to map intensities (after interfering the probe with the LO) onto phase changes of the probe. Note that the intensity of the recalled probe does not depend on whether or not a signal is present, i.e. the calibration, taken without any signal, remains valid when the signal is actually present. Note that for these sets of measurements, MEMS1 is used in a configuration where it directs light from the output of the waveguide directly to the detector.

Eq. 4.2 predicts that for a given detuning, the phase shift on the probe increases linearly with the number of photons in the signal. To verify this, we vary the mean number of photons constituting the signal pulse from 0 to over 10^8. The total phase shift for each mean photon number is measured by averaging over 200 repetitions. For example, consider the case where we set the signal detuning to +100 MHz, as shown in the right inset of Fig. 4.8, and vary the mean photon number per pulse in regular intervals from 0 to 1.7×10^8. As expected from Eq. 4.2, we find a linear increase in the total phase shift as a function of the number of signal photons. Fitting a straight line to this lets us estimate the average phase shift per photon, which is of the order 10^{-9} radians per photon. We repeat the above procedure for nine different detunings, including three negative detunings. Note that the slope for negative detuning is opposite to that of positive detuning, hence giving an increasingly negative total phase shift as a function of total number of photons. and estimate the phase shift per photon in each case, as shown in Fig. 4.8.

To compare the measured values of phase shift to the theoretical predictions, we use Eq. 4.2

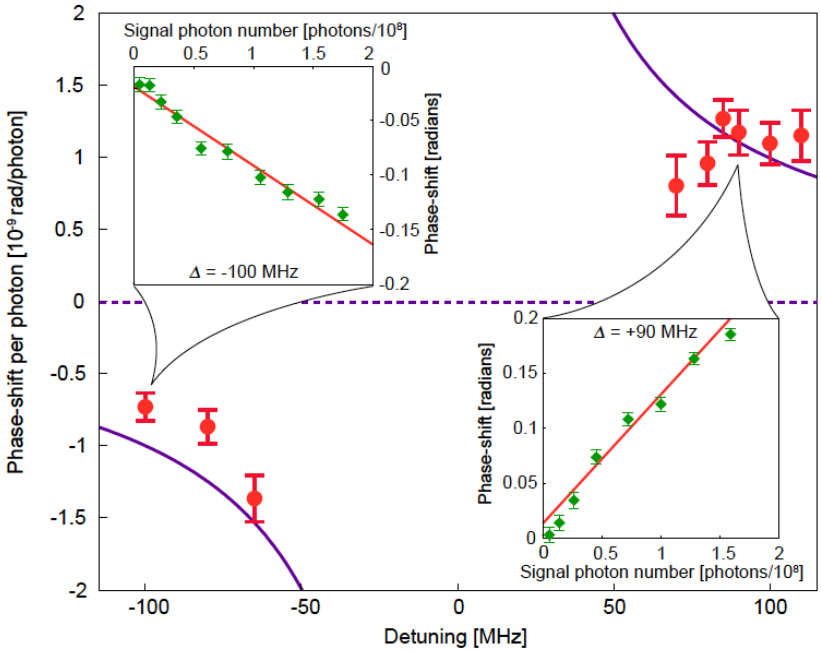

Figure 4.8: Phase shift per photon for different detuning values. Expected phase shifts (purple line) calculated using Eq. 4.2 with independently measured quantities (no fit), and experimentally obtained values (red circles) derived from linear fits to the phase shift versus mean photon number as illustrated in the insets for two detuning values (red lines). Uncertainty bars on the red data points are based on the standard deviation of the slope from the linear fits. Each data point in the insets (green diamonds) corresponds to an average over 200 repetitions and the uncertainty bars indicate the standard deviation of the average. Figure taken from [1].

with λ=795 nm, n=2.3, A=$\pi\times(6.25\ \mu\text{m})^2$ and γ=8.1 kHz. We plot the theoretically expected values in Fig. 4.8 (purple line), confirming that the measured values of phase shift are in good agreement with the theoretical predictions. In particular, at +100 MHz detuning, we measure a phase shift of $(1.10 \pm 0.14) \times 10^{-9}$ rad per photon, which is in excellent agreement with the expected value of 1.0×10^{-9} rad per photon. Discrepancies between measured and predicted values are most likely due to imperfections in the tailored atomic absorption spectrum and in the spectrum of signal pulses that arise when the AOM is driven with signals that approach or exceed the AOM's bandwidth limit. We also note that there is some uncertainty on the parameters — such as the waveguide cross-sectional area and fibre-to-waveguide coupling loss — that go into this estimate.

The precision of the phase measurements is mainly limited by long-term laser frequency instability. To reduce its impact, we concatenate each measurement of the AC Stark shift on the probe

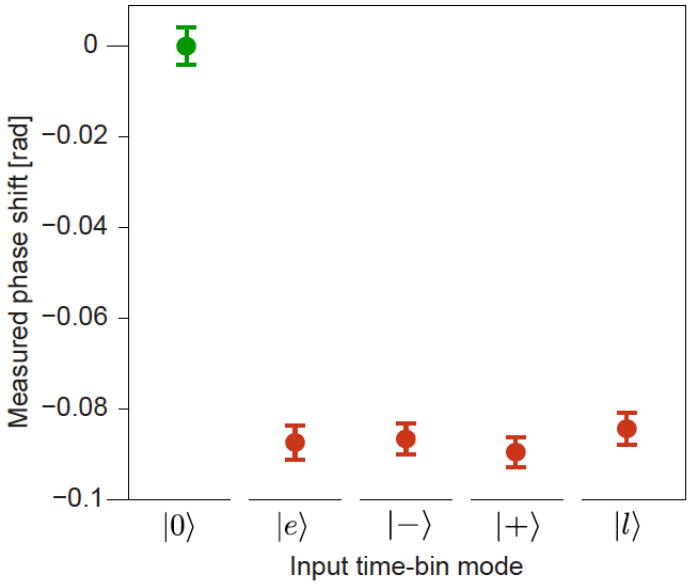

Figure 4.9: Phase shifts for different signal pulses. Probe phase shifts due to 6.9×10^7, or no, signal photons, distributed between early and late temporal modes. The labels on the x-axis refer to either no signal photons ($|0\rangle$) or the corresponding time-bin qubit states, where $|e\rangle$ and $|l\rangle$ refer to qubits prepared in early and late temporal modes, respectively, and $|+\rangle$ and $|-\rangle$ represent the superposition states $(|e\rangle+|l\rangle)/\sqrt{2}$ and $(|e\rangle-|l\rangle)/\sqrt{2}$, respectively. Each data point shows the average over 1000 measurements, and uncertainty bars denote the standard deviation of the average. Figure taken from [1].

with a reference measurement of the probe's phase without a signal (see Fig. 4.6). Subtracting the value obtained in the second phase measurement from the first allows improving the single-shot phase sensitivity. The sensitivity can be further improved laser locking, which limits laser frequency fluctuations between the generation of the probe and LO pulses.

4.4.6 Signal in a time-bin qubit state

For our measurement to qualify as a proof-of-principle demonstration of a non-destructive measurement, it needs to confirm two main criteria: (i) the probe phase shift is independent of how the photons constituting the signal are distributed between two temporal modes, and (ii) the signal is not affected by the measurement. Put into the context of an interaction with a single photon in a time-bin qubit state, this implies that the measurement does not project the qubit onto a specific set of basis states and thus alter it. Towards this end, we select early and late signal modes, each

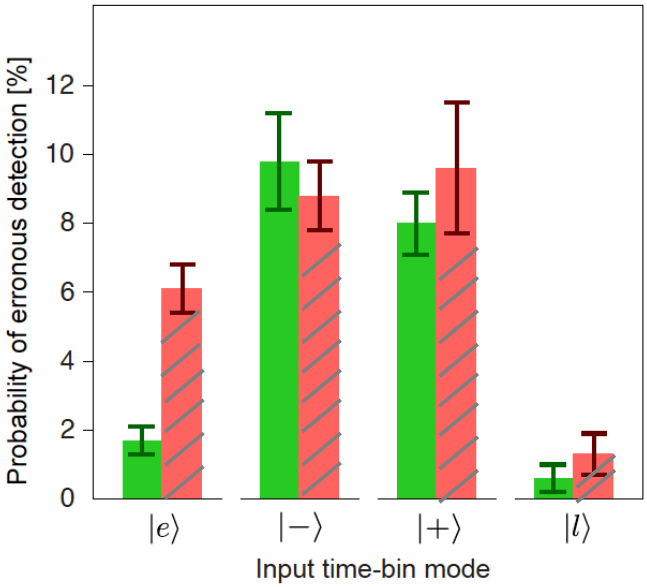

Figure 4.10: Error rates for different signal pulses. The error rates — the ratio of the energy detected in the wrong output mode to the total energy detected in both the correct and wrong modes — of the different signal states before (unshaded) and after (shaded) the measurement. Error bars are calculated from shot-to-shot pulse-heights variations. There is no significant change, except for $|e\rangle$. Figure taken from [1].

of 10 ns duration, separated by 18.3 ns, and featuring a detuning of +100 MHz. Keeping the total number of photons constant, we do our measurement with the following four signals: (i) all the photons are in the early mode, (ii) all the photons are in the late mode, (iii) the photons are in an equal superposition of early and late modes with a phase difference of 0 (called '+' state), and (iv) the photons are in an equal superposition of early and late modes with a phase difference of π (called '-' state). The resulting probe phase shifts, averaged for each pulse sequence over 1000 repetitions, are plotted in Fig. 4.9, which also includes the phase shift measured without a signal pulse. We find that, within experimental uncertainty, the phase shifts are the same irrespective of the signal state, and that they clearly differ from the phase shift measured without any signal.

Next, we need to verify that our measurement preserves the signal state. The variation of the signal due to the interaction with the probe is assessed as follows: for early and late signal states we measure the pulse heights in the wrong time bin, normalized to the sum of the pulse heights in both bins. For the superposition states, we pass the signal through an unbalanced fibre

interferometer whose arm-length difference corresponds to 18.3 ns travel-time difference. Using a piezoelectric transducer in one arm of the interferometer, we set its phase to obtain maximum constructive interference in one output, and record the normalized pulse heights in the other (the wrong) output. All measurements are done twice — once before, and once after the signal is submitted to the cross-phase interaction. Differences in the results indicate the perturbation of the signal due to the measurement. As shown in Fig. 4.10, we find close to no change due to the cross-phase interaction, except for $|e\rangle$. Increased errors in $|e\rangle$ are likely due to free induction decay after the signal pulse excites remaining thulium atoms inside the pit, and would disappear with better hole burning. As the decay happens after absorption, only $|e\rangle$ is affected. Errors for the superposition states are caused by imperfections in the interferometer, and are hence similar with and without the measurement. Thus we conclude that our scheme measures the presence of a time-bin qubit without revealing, nor modifying, its state.

Chapter 5

Conclusion and outlook

Our proof-of-principle demonstration confirms the two key features of our proposal: (i) that we obtain the expected cross-phase modulation, and (ii) that the signal is not modified due to our measurement. However, a lot remains to be done to non-destructively detect qubits encoded into individual photons. This would entail increasing the phase-shift per photon from the current value of about 1 nrad. The first step towards this end could be to reduce the interaction cross section area. We expect that, using for example a small-diameter ridge waveguide, the phase sensitivity can be increased by more than a factor of 100. Additionally, the ratio between the radiative lifetime γ and the detuning Δ has to be increased beyond its current value of 8.1 kHz/($2\pi\times$65 MHz)$\sim 2\times 10^{-5}$. This ratio can in principle approach one percent.

However, reducing the detuning to maximize γ/Δ comes with the unwanted effects of increasing off-resonant absorption of the signal in the AFC increasing the noise due to decay from excited atoms, and decreasing the bandwidth of the signal. However, as we discussed in Chapter. 3, these problems can be overcome in a configuration in which the population in the excited state (populated through the absorption of the strong probe in the AFC) is temporarily transferred to an auxiliary level, and in which the signal passes many times through the spectral pit during the storage of the probe. This makes it possible to increase the detuning and thus reduce the absorption of the signal without decreasing the total phase shift experienced by the probe. For instance, we anticipate non-destructive measurement to be feasible using an AFC with teeth of optical depth 30 [35] and signal photons of half a MHz bandwidth that interact approximately 900 times with the stored probe, which corresponds to the use of a moderate-finesse cavity. With these improvements, the phase shift per photon could thus be as large as 0.1 mrad, which would allow single-shot detection of individual photons [48].

We emphasize that the cross-phase interaction in rare-earth-ion doped crystals is straightforward to generalize to multiple spectral channels, as demonstrated in the context of AFC-based optical quantum memory [38], which can extend over a total bandwidth of hundreds of GHz [41]. We also note that the present approach should allow the development of a standard (destructive) photon-number-resolving detector, for which the limitations imposed by signal loss and noise are less severe.

We believe that an improved version of our proof-of-principle demonstration will soon allow first destructive, and then non-destructive, single shot detection of photons. This will open the path to more efficient use of precious probabilistic resources, such as entangled photons, in advanced applications of quantum communication. Furthermore, it will allow the heralded generation of photon-number states, including entangled states, that do not contain often detrimental admixtures of undesired photons as, e.g., in widely-used spontaneous parametric down-conversion [49].

Appendix A

Appendix

A.1 Cross-phase modulation due to signal

The total Hamiltonian that governs the dynamics due to the presence of the signal field is given by

$$\hat{H}_{\text{tot}} = \hat{H}_0 + \hat{H}_{\text{int}} = \sum_{j=1}^{N} \hbar\omega_{\text{ge}}^{j}\sigma_{\text{ee}}^{j} + \hat{h}_{\text{int}}^{j}, \tag{A.1}$$

where

$$\hat{h}_{\text{int}}^{j} = -\hbar g\sqrt{\frac{L}{2\pi c}}\int d\omega \hat{a}_{\omega} e^{i\omega z_j/c}\hat{\sigma}_{\text{eg}}^{j} + \text{H.c.}. \tag{A.2}$$

The transition frequency of the j^{th} atom is ω_{eg}^{j}, and the atomic coherence and population operators are denoted by $\hat{\sigma}_{\nu\nu'}^{j} = |\nu\rangle^{j}\langle\nu'|$, where $\nu,\nu' = \{g,e\}$. $\hat{a}_{\omega}$ is the anihilation operator for signal field modes and the single photon coupling is given by $g = \mu_{\text{eg}}\sqrt{\frac{\omega_s}{2\hbar\varepsilon V}}$, where ω_s is the central frequency of the signal, and the transition dipole moment is $\mu_{\text{eg}} = \langle e|\mathbf{d}\cdot\boldsymbol{\varepsilon}_s|g\rangle$. Throughout this analysis, we assume that $\omega_p = \omega_0$, where ω_0 is the central frequency of the AFC.

We use the collective atomic operators that are defined in Eqs. 3.4, 3.5 and 3.6 to re-write the interaction Hamiltonian in Eq. A.2. This results in

$$\hat{H}_{\text{int}} = -\hbar g\sum_{j=1}^{N}\sqrt{\frac{L}{2\pi c}}e^{i\omega_p(t-z_j/c)}\int d\omega \hat{a}_{\omega}e^{i\omega z_j/c}\hat{\sigma}_{\text{eg}}^{j}e^{-i\omega_p(t-z_j/c)} + H.c., \tag{A.3}$$

which leads to

$$\hat{H}_{\text{int}} = -\hbar g\int dz n_z(\delta)e^{i\Delta(t-z/c)}\hat{\mathscr{E}}_s(z,t)\hat{\sigma}_{\text{eg}}(z,t;\delta) + H.c, \tag{A.4}$$

where

$$\hat{\mathscr{E}}_s(z,t) = \sqrt{\frac{L}{2\pi c}}e^{i\omega_s(t-z/c)}\int d\omega \hat{a}_{\omega}e^{i\omega z/c}, \tag{A.5}$$

$n_z(\delta)dz = N_z(\delta)$, $\int dz n_z(\delta) = N(\delta)$ and $\Delta = \omega_p - \omega_s$ is the detuning between the signal and probe fields.

Using the effective interaction Hamiltonian we derive the dynamical equation for the collective atomic polarization.

$$\dot{\hat{\sigma}}_{\rm eg}(z,t;\delta) = \frac{i}{\hbar}\left[\hat{H}_0 + \hat{H}^{\rm eff}_{\rm int}, \hat{\sigma}_{\rm eg}(z,t;\delta)\right] + \frac{\partial \hat{\sigma}_{\rm eg}(z,t;\delta)}{\partial t}.$$

This leads to

$$\dot{\hat{\sigma}}_{\rm eg}(z,t;\delta) = i\delta\hat{\sigma}_{\rm eg}(z,t;\delta) + \frac{2ig^2}{\Delta}\left(\hat{\mathscr{E}}_s(z,t)\hat{\mathscr{E}}_s^{\dagger}(z,t) + H.c.\right)\hat{\sigma}_{\rm eg}(z,t;\delta), \tag{A.6}$$

and consequently

$$\hat{\sigma}_{\rm eg}(z,t=T_2;\delta) = e^{i\delta t}e^{i\hat{\Phi}}\hat{\sigma}_{\rm eg}(z,t=T_1;\delta), \tag{A.7}$$

where

$$\hat{\Phi} = \int_{T_1}^{T_2} dt' \frac{2g^2}{\Delta}\left(\hat{\mathscr{E}}_s(z,t')\hat{\mathscr{E}}_s^{\dagger}(z,t') + \hat{\mathscr{E}}_s^{\dagger}(z,t')\hat{\mathscr{E}}_s(z,t')\right). \tag{A.8}$$

A.2 Signal loss

To analyze the signal loss, we treat the signal propagation using the Maxwell equation as follows

$$\left(\partial_z + \frac{n}{c}\partial_t\right)\hat{\mathscr{E}}_s(z,t) = \frac{\mu_0\omega_0^2\mu_{\rm eg}}{2k_0}\sum_{\delta}\frac{N(\delta)}{V}\hat{\sigma}_{\rm eg}(z,t;\delta), \tag{A.9}$$

where $k_0 = \frac{n\omega_0}{c}$. Given that the equations governing the single-excitation wave functions are the same as the Maxwell-Bloch equations, for evaluating the signal loss, we take Fourier transform of the Maxwell-Bloch equations for single-excitation wavefunctions. As a result the output signal wave function in the frequency domain is given by

$$\tilde{\mathscr{E}}_s(z,\omega)|_{z=L} = e^{ik_s\chi(\omega)L}\tilde{\mathscr{E}}_s(z=0,\omega), \tag{A.10}$$

where

$$\chi(\omega) = \frac{1}{k_s}\left(-\frac{n\omega}{c} + \frac{\mu_0\omega_0^2\mu_{\rm eg}}{2k_0}\sum_{\delta}\frac{N(\delta)}{V}\frac{i\mu_{\rm eg}/2\hbar}{i(\omega-(\Delta+\delta))-\gamma}\right), \tag{A.11}$$

and $k_s = \frac{n\omega_s}{c}$. The imaginary part of $\chi(\omega)$ determines the loss. We can simplify the above expression by assuming $\Delta \gg \Gamma$, where $-\Gamma/2 < \delta < \Gamma/2$. In addition, the loss is expected to be uniform

over the signal field spectrum when its bandwidth is smaller than the detuning ($\Delta \gg 1/\tau_s$). This results in a rather simple expression for the imaginary part of the response function, $\chi(\omega)$. For $\Delta \gg \gamma$, it is given by

$$\mathrm{Imag}(\chi(0)) = \frac{1}{k_s}\frac{1}{16\pi}\frac{N_g\lambda_0^2\gamma^2}{n^2V\Delta^2}. \tag{A.12}$$

Therefore, the intensity loss for the signal field can be derived from

$$|\mathscr{E}(L,\omega)|^2 = e^{-\zeta L}|\mathscr{E}(0,\omega)|^2, \tag{A.13}$$

where

$$\zeta L = \frac{1}{8\pi}\frac{N_g\lambda_0^2}{n^2A}\frac{\gamma^2}{\Delta^2}. \tag{A.14}$$

Bibliography

[1] Sinclair, N. *et al.* Proposal and proof-of-principle demonstration of non-destructive detection of photonic qubits using a Tm:$LiNbO_3$ waveguide. *Nat. Commun.* **7**, 13454 (2016).

[2] Feynman, R. P. Simulating physics with computers. *Int. J. Theor. Phys.* **21**, 467–488 (1982).

[3] Gisin, N. & Thew, R. Quantum communication. *Nat. Photon.* **1**, 165–171 (2007).

[4] Gisin, N., Ribordy, G., Tittel, W. & Zbinden, H. Quantum cryptography. *Rev. Mod. Phys.* **74**, 145 (2002).

[5] Giovannetti, V., Lloyd, S. & Maccone, L. Quantum-enhanced measurements: beating the standard quantum limit. *Science* **306**, 1330–1336 (2004).

[6] Giovannetti, V., Lloyd, S. & Maccone, L. Advances in quantum metrology. *Nat. Photon.* **5**, 222–229 (2011).

[7] Kimble, H. J. The quantum internet. *Nature* **453**, 1023–1030 (2008).

[8] Knill, E., Laflamme, R. & Milburn, G. J. A scheme for efficient quantum computation with linear optics. *Nature* **409**, 46–52 (2001).

[9] Duan, L. M., Lukin, M. D., Cirac, J. I. & Zoller, P. Long-distance quantum communication with atomic ensembles and linear optics. *Nature* **414**, 413–418 (2001).

[10] Nemoto, K. & Munro, W. J. Nearly deterministic linear optical controlled-not gate. *Phys. Rev. Lett.* **93**, 250502 (2004).

[11] Bennett, C. H. *et al.* Teleporting an unknown quantum state via dual classical and Einstein-Podolsky-Rosen channels. *Phys. Rev. Lett.* **70**, 1895 (1993).

[12] Sangouard, N., Simon, C., De Riedmatten, H. & Gisin, N. Quantum repeaters based on atomic ensembles and linear optics. *Rev. Mod. Phys.* **83**, 33 (2011).

[13] Imoto, N., Haus, H. & Yamamoto, Y. Quantum nondemolition measurement of the photon number via the optical Kerr effect. *Phys. Rev. A* **32**, 2287 (1985).

[14] Reiserer, A., Ritter, S. & Rempe, G. Nondestructive detection of an optical photon. *Science* **342**, 1349–1351 (2013).

[15] Kalb, N., Reiserer, A., Ritter, S. & Rempe, G. Heralded storage of a photonic quantum bit in a single atom. *Phys. Rev. Lett.* **114**, 220501 (2015).

[16] Fleischhauer, M., Imamoglu, A. & Marangos, J. P. Electromagnetically induced transparency: Optics in coherent media. *Rev. Mod. Phys.* **77**, 633 (2005).

[17] Tiarks, D., Schmidt, S., Rempe, G. & Dürr, S. Optical π phase shift created with a single-photon pulse. *Sci. Adv.* **2**, e1600036 (2016).

[18] Saffman, M., Walker, T. & Mølmer, K. Quantum information with Rydberg atoms. *Rev. Mod. Phys.* **82**, 2313 (2010).

[19] Beck, K. M., Hosseini, M., Duan, Y. & Vuletić, V. Large conditional single-photon cross-phase modulation. *Proc. Nat. Acad. Sci.* **113**, 9740–9744 (2016).

[20] Schmidt, H. & Imamoglu, A. Giant kerr nonlinearities obtained by electromagnetically induced transparency. *Opt. Lett.* **21**, 1936–1938 (1996).

[21] Hammerer, K., Sørensen, A. S. & Polzik, E. S. Quantum interface between light and atomic ensembles. *Rev. Mod. Phys.* **82**, 1041 (2010).

[22] Hosseini, M., Beck, K. M., Duan, Y., Chen, W. & Vuletić, V. Partially nondestructive continuous detection of individual traveling optical photons. *Phys. Rev. Lett.* **116**, 033602 (2016).

[23] Chang, D. E., Vuletić, V. & Lukin, M. D. Quantum nonlinear optics - photon by photon. *Nat. Photon.* **8**, 685–694 (2014).

[24] Gorshkov, A. V., Otterbach, J., Fleischhauer, M., Pohl, T. & Lukin, M. D. Photon-photon interactions via Rydberg blockade. *Phys. Rev. Lett.* **107**, 133602 (2011).

[25] Dudin, Y. & Kuzmich, A. Strongly interacting Rydberg excitations of a cold atomic gas. *Science* **336**, 887–889 (2012).

[26] Firstenberg, O. *et al.* Attractive photons in a quantum nonlinear medium. *Nature* **502**, 71–75 (2013).

[27] Feizpour, A., Hallaji, M., Dmochowski, G. & Steinberg, A. M. Observation of the nonlinear phase shift due to single post-selected photons. *Nat. Phys.* **11**, 905–909 (2015).

[28] Venkataraman, V., Saha, K. & Gaeta, A. L. Phase modulation at the few-photon level for weak-nonlinearity-based quantum computing. *Nat. Photon.* **7**, 138–141 (2013).

[29] Tiarks, D., Baur, S., Schneider, K., Dürr, S. & Rempe, G. Single-photon transistor using a Förster resonance. *Phys. Rev. Lett.* **113**, 053602 (2014).

[30] Chen, W. *et al.* All-optical switch and transistor gated by one stored photon. *Science* 1237242 (2013).

[31] Afzelius, M., Simon, C., de Riedmatten, H. & Gisin, N. Multimode quantum memory based on atomic frequency combs. *Phys. Rev. A* **79**, 052329 (2009).

[32] Zhong, M. *et al.* Optically addressable nuclear spins in a solid with a six-hour coherence time. *Nature* **517**, 177–180 (2015).

[33] Bussières, F. *et al.* Quantum teleportation from a telecom-wavelength photon to a solid-state quantum memory. *Nat. Photon.* **8**, 775–778 (2014).

[34] Gündoğan, M., Ledingham, P. M., Kutluer, K., Mazzera, M. & de Riedmatten, H. Solid state spin-wave quantum memory for time-bin qubits. *Phys. Rev. Lett.* **114**, 230501 (2015).

[35] Hedges, M. P., Longdell, J. J., Li, Y. & Sellars, M. J. Efficient quantum memory for light. *Nature* **465**, 1052–1056 (2010).

[36] Clausen, C. *et al.* Quantum storage of photonic entanglement in a crystal. *Nature* **469**, 508–511 (2011).

[37] Saglamyurek, E. *et al.* Broadband waveguide quantum memory for entangled photons. *Nature* **469**, 512–515 (2011).

[38] Sinclair, N. *et al.* Spectral multiplexing for scalable quantum photonics using an atomic frequency comb quantum memory and feed-forward control. *Phys. Rev. Lett.* **113**, 053603 (2014).

[39] Saglamyurek, E. *et al.* An integrated processor for photonic quantum states using a broadband light matter interface. *New J. Phys.* **16**, 065019 (2014).

[40] Allen, L. & Eberly, J. H. *Optical resonance and two-level atoms* (Courier Corporation, 2012).

[41] Sun, Y., Thiel, C. & Cone, R. Optical decoherence and energy level structure of 0.1% Tm:$LiNbO_3$. *Phys. Rev. B* **85**, 165106 (2012).

[42] Gea-Banacloche, J. Impossibility of large phase shifts via the giant kerr effect with single-photon wave packets. *Phys. Rev. A* **81**, 043823 (2010).

[43] Macfarlane, R. & Shelby, R. Coherent transient and holeburning spectroscopy of rare earth ions in solids. *Spectroscopy of solids containing rare earth ions* **21** (1987).

[44] Dirac, P. A. M. The Quantum Theory of the Emission and Absorption of Radiation. *Proc. R. Soc. London, Ser. A* **114**, 243–265 (1927).

[45] Sinclair, N. *et al.* Spectroscopic investigations of a ti:tm:$linbo_3$ waveguide for photon-echo quantum memory. *J. Lumin.* **130**, 1586–1593 (2010).

[46] Sinclair, N., Oblak, D., Thiel, C. W., Cone, R. L. *et al.* A rare-earth-ion-doped waveguide based on a standard photonics technology for quantum signal processing. *arXiv:1605.02396* (2016).

[47] Thiel, C., Sun, Y., Bõttger, T., Babbitt, W. & Cone, R. Optical decoherence and persistent spectral hole burning in tm3+:linbo3. *J. Lumin.* **130**, 1598 – 1602 (2010).

[48] Appel, J. *et al.* Mesoscopic atomic entanglement for precision measurements beyond the standard quantum limit. *Proc. Nat. Acad. Sci.* **106**, 10960–10965 (2009).

[49] Guha, S. *et al.* Rate-loss analysis of an efficient quantum repeater architecture. *Phys. Rev. A* **92**, 022357 (2015).